ISSN (Print) 1226-1750
ISSN (Online) 2233-6656
**Journal of Magnetics** 27(3), 286-292 (2022) https://doi.org/10.4283/JMAG.2022.27.3.286

# Synthesis and Electromagnetic Wave Absorbing Properties of Ni-substituted Z-type Hexaferrite-epoxy Composites

**Young-Min Kang[1], Jin-Young You[1], and Sang-Min Lee[2]***

[1]*Department of Materials Science and Engineering, Korea National University of Transportation, Chungju 27469, Republic of Korea*
[2]*Division of Creative Convergence, Korea National University of Transportation, Chungju 27469, Republic of Korea*

(Received 3 June 2022, Received in final form 3 August 2022, Accepted 4 August 2022)

**Ni-substituted Z-type hexaferrites with the chemical formula $Sr_3Co_{2-x}Ni_xFe_{24}O_{41}$ ($x$ = 0, 0.1, 0.2, 0.3, 0.4, 0.5) were prepared by solid-state reaction processes. XRD analysis revealed that nearly a single Z-type hexaferrite phase could be obtained for the samples with Ni substitution $x \leq 0.5$ when the samples were twice calcined at 1160 and 1235 °C, respectively, in air. The complex permittivity ($\varepsilon'$, $\varepsilon''$) and permeability ($\mu'$, $\mu''$) spectra (100 MHz $\leq f \leq$ 18 GHz) and electromagnetic (EM) wave absorption properties were studied on $Sr_3Co_{2-x}Ni_xFe_{24}O_{41}$ ($x$ = 0, 0.1, 0.2, 0.3, 0.4, 0.5) powder-epoxy (10 wt%) composites. The permeability spectra continuously shifted to a lower frequency with an increase in $x$, owing to the decrease in the magnetocrystalline anisotropy. The peak frequency of $\mu''$ gradually decreased from 3.2 GHz to 2.0 GHz, and in turn, it shifted the corresponding EM absorption frequency range. The frequency corresponding to the minimum RL peak point also decreased from 3.3 GHz to 2.3 GH with an increase in $x$ from 0 to 0.5. All the samples exhibited the lowest reflection loss of < -40 dB at the optimized frequency and thickness. The study shows that Ni substitution is very effective for the delicate tuning of electromagnetic absorption frequency in S-band (2-4 GHz).**

**Keywords :** Z-type hexaferrite, EM wave absorption, permeability, permittivity, reflection loss

## 1. Introduction

Z-type hexaferrite ($Ba_3Co_2Fe_{24}O_{41}$ or $Sr_3Co_2Fe_{24}O_{41}$), which is one of the six hexaferrite groups (M, Z, Y, W, X, and U types), has been studied in recent decades because of its attractive physical properties, including its high planar magnetic anisotropy and permeability up to the gigahertz range [1, 2]. These properties make it applicable to RF and microwave devices such as electromagnetic (EM) wave absorbers [3, 4], antennas [5-8], and chip inductors [9] that operate in a gigahertz range. $Ba_3Co_2Fe_{24}O_{41}$ ($Ba_3Co_2Z$) has a saturation magnetization of 43-51 emu/g at room temperature and Curie temperature of ~690 K [2]. It also has a static magnetic permeability ($\mu_S$) of 8-20 and ferromagnetic resonance (FMR) frequency of 1.5 GHz [1, 3, 10], and it exhibits $c$-plane anisotropy with an in-plane anisotropy field of $H_\theta$ ~0.12 kOe, which is much smaller than the $c$-axis anisotropy field ($H_\Phi$ ~12 kOe). Thus, the magnetic easy axis lies parallel to the basal plane [11].

EM wave-absorbing materials in the form of magnetic particles employed in polymer matrices are generally studied because they are desirable for real applications due to their high formability. Recently, improved EM absorbing properties at GHz range through designing the nanocomposites where magnetic nanoparticles were employed in template materials have been reported [12-15]. In the studies, high EM absorption performances with a relatively broad absorption bandwidth could be achieved through controlling the morphology, porosity, and core-shell structures of particles and thus its complex permittivity and permeability properties. Z-type hexaferrites have an FMR frequency ($f_{FMR}$) in the range of 1-4 GHz and very low dielectric loss properties, making them suitable for radar-absorbing material applications. To adjust the EM wave absorption frequency band of Z-type hexaferrites, $f_{FMR}$ should be gradually controlled through proper cation substitution. When EM waves are irradiated to a material, the absorption, reflection, and transmission of the EM waves depend on the material properties, including its permittivity and permeability, which are complex numbers expressed in the form of $\varepsilon = \varepsilon' - j\varepsilon''$ and


*Corresponding author: Tel: +82-43-849-1667
Fax: +82-43-841-5685, e-mail: leesm@ut.ac.kr

$\mu = \mu' - j\mu''$, respectively. The imaginary parts of permittivity ($\varepsilon''$) and permeability ($\mu''$) are related to EM wave absorption through dielectric and magnetic loss mechanisms. In addition, good impedance matching characteristics that are functions of these $\varepsilon'$, $\varepsilon''$, $\mu'$, $\mu''$ material parameters are crucial for high EM wave absorbing performance without high EM wave reflection [13]. Previous studies have shown that the magnetic loss that occurs when $\mu''$ increases due to FMR is the dominant EM wave absorption mechanism in hexaferrites in the GHz range [17-23].

It has also been reported that partial substitution of $Co^{2+}$ by $Zn^{2+}$ can effectively modify the magnetic anisotropy of $Ba_3Co_2Z$ ferrite. The anisotropy of Z-type $Ba_3Co_xZn_{2-x}Fe_{24}O_{41}$ ferrite changes from a *c*-plane to a *c*-axis type at $x$ = 1.2-1.6 [24]. In our previous research [10], $f_{FMR}$ of the $Sr_3Co_{2-x}Zn_xFe_{24}O_{41}$ ($x$ = 0, 0.5, 1.0, 1.5)-epoxy composites could be controlled from 3.4 to 1.1 GHz. Thus, the EM absorbing band can also be adjusted based on the change in $f_{FMR}$. In another study [23], the EM absorption mechanism was studied in highly pure $Sr_3Co_2Z$ powder-epoxy composites, where $Sr_3Co_2Z$ powders were prepared by the sol-gel method. The study revealed that the EM absorption frequency band could be controlled by an external magnetic field ($H_{ex}$) because the $f_{FMR}$ of the $Sr_3Co_2Z$ increased gradually with an increase in $H_{ex}$.

In the phase diagram of BaO-$Fe_2O_3$-MeO constructed by Vinnik [25], the Z-phase is located in the middle of other hexaferrite compositions and is compatible with the aforementioned phases (M, U, Y, and W). Therefore, the synthesis of a pure Z hexaferrite phase is very difficult [1, 2]. Furthermore, the process window for $Sr_3Co_2Z$ is narrower than that for $Ba_3Co_2Z$, and therefore its synthesis is much more difficult [26, 27]. Because of this problem, sufficient research on cation substitution of $Sr_3Co_2Z$ has not been conducted. In this study, Ni, which is a magnetic element, was used to replace the Co site in $Sr_3Co_2Z$, and, accordingly, the change in the EM wave absorption characteristics was investigated. To the best of our knowledge, no studies on the EM wave absorption characteristics of Ni-substituted $Sr_3Co_2Z$ have been reported. First, when Ni-substituted $Sr_3Co_2Z$ was synthesized in air using a solid-state reaction method, the optimal calcination temperature with Ni up to maximum content was investigated. The crystal structure, microstructure, high-frequency permittivity and permeability characteristics, and EM wave absorption characteristics were then studied based on the substitution of Ni.

## 2. Experimental Procedure

Z-type hexaferrites with the formula $Sr_3Co_{2-x}Ni_xFe_{24-\delta}O_{41}$ ($x$ = 0.0, 0.1, 0.2, 0.3, 0.4, 0.5, 1.0, and $d$ = 1.0) were prepared by conventional solid-state reaction processes. Precursor powders of $Fe_2O_3$ (Kojundo Chemical, 99.5 %), $SrCO_3$ (Kojundo Chemical, 99.5 %), $Co_3O_4$ (Kojundo Chemical, 99.5 %), and NiO (99 %, Junsei Chemical) were weighed according to the cation ratios of the formula. Based on our previous research, an Fe-deficient ($\delta$ = 1) nominal cation composition $Sr_3Co_2Fe_{23}$ was used to obtain a purer Z-type phase [28]. The powder mixture was ball-milled in water for 20 h using a polypropylene jar and yttria-stabilized $ZrO_2$ balls with diameters of 3, 5, and 10 mm. The dried slurry was precalcined at 1160 °C in air for 4 h. The precalcined powders were calcined again in air at temperatures of 1185, 1210, 1235, and 1250 °C for 2 h. The second calcined powders were ground again and then mixed with 10 wt% of an epoxy binder (YD014, Kukdo Chemical), pressed into toroidal-shaped green compacts (with inner and outer diameters of 3.04 and 7.00 mm, respectively, and thickness 3.0 mm), and finally cured at 180 °C for 1 h in air.

X-ray diffraction (XRD, D8 Advance, Bruker) with a Cu $K_\alpha$ radiation source ($\lambda$ = 0.154056 nm) was used for crystalline phase analysis. Field-emission scanning electron microscopy (JSM-7610F, JEOL) was used for microstructural observation of the second set of calcined samples. The complex permittivity and permeability spectra (100 MHz-18 GHz) of the toroidal hexaferrite-epoxy composites were measured using a vector network analyzer (E5063A, Keysight) with an airline kit (85051BR03) and N1500A software. Reflection losses (RLs) of the composites were calculated using the permittivity and permeability spectra.

## 3. Results and Discussion

Figure 1(a)-(d) show the XRD patterns of Ni-substituted Z-type hexaferrites ($Sr_3Co_{2-x}Ni_xFe_{23}O_{41}$) calcined at 1185-1250 °C. In a previous study, the optimal second calcination temperature ($T_{cal}$) for the preparation of Zn-substituted $Sr_3Co_2Z$, $Sr_3Co_{2-x}Zn_xFe_{24}O_{41}$ ($x$ = 0, 0.5, 1.0, 1.5) synthesized by a solid-state reaction was 1210 °C [10]. Fig. 1(b) confirms that nearly a single Z-type phase could be obtained at $T_{cal}$ = 1210 °C for $x$ = 0 and $x$ = 0.3. However, a large amount of the M-type phase was formed as the primary phase at $x$ = 0.5, and the W-type phase became the primary phase at $x$ = 1.0. When the $T_{cal}$ was lowered to 1185 °C, as shown in Fig. 1(a), the M and Z phases coexisted with a spinel (S) phase for both $x$ = 0.5 and 1.0 samples. As Fig. 1(c) shows, Ni-substituted $Sr_3Co_2Z$ was best formed at $T_{cal}$ = 1235 °C. The $x$ = 0.5 sample showed nearly a single Z-type phase. The $x$ = 1.0 sample

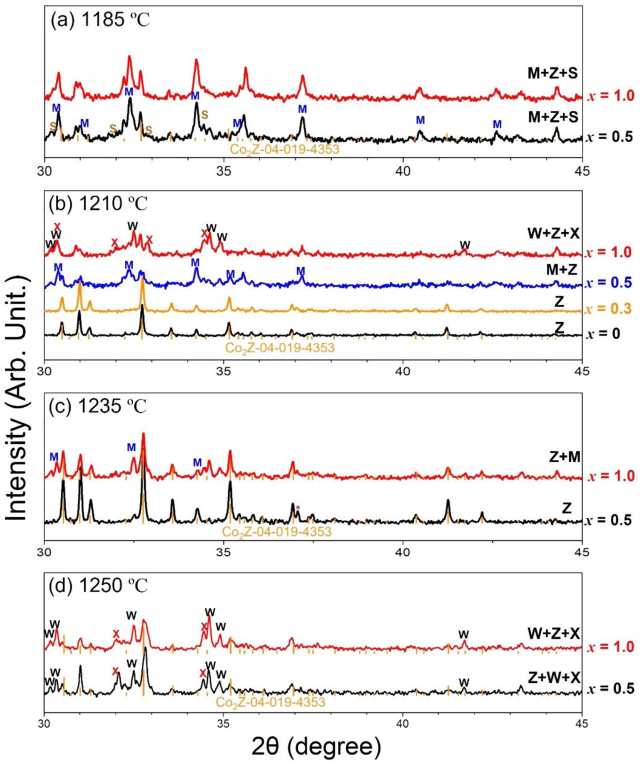


**Fig. 1.** (Color online) XRD patterns of Ni-substituted Z-type hexaferrites ($Sr_3Co_{2-x}Ni_xFe_{23}O_{41}$) calcined at 1185, 1210, 1235, and 1250 ℃.

also had a Z-type phase as the primary phase with an M-phase as the second. When the $T_{cal}$ increased to 1250 °C, a large amount of W and X phases formed in the $x$ = 0.5 and $x$ = 1.0 samples. It is because W and X phases become more stable at a high temperature (≥1250 °C) than Z phase. The W and X phases lie on the tie-line in the phase diagram, and thus the two phases can coexist [25]. Similar results have been reported in our previous study [23].

The XRD patterns of the Ni-substituted $Sr_3Co_2Z$ samples calcined at 1235 °C with a Ni substitution level $x$ from 0 to 0.5 are presented in Fig. 2. The diffraction peaks of the samples were indexed based on $Co_2Z$ with a hexagonal structure (International Center for Diffraction Data (ICDD), pdf search no. 04-019-4353). All samples showed nearly a single Z-phase. Although the peak at 2θ ≈ 37º (indicated by an asterisk *) did not match the ICDD patterns of the Z-type phase, it was nevertheless believed to have originated from the Z-phase based on previous experimental results [23, 30, 31]. Another unmatched peak at 2θ ≈ 32.5º corresponded to the main peak of the M-type phase. The XRD results showed that the solubility of Ni ($x$) in the $Sr_3Co_2Z$ phase was the highest at $T_{cal}$ of 1235 °C. Therefore, all subsequent experiments were

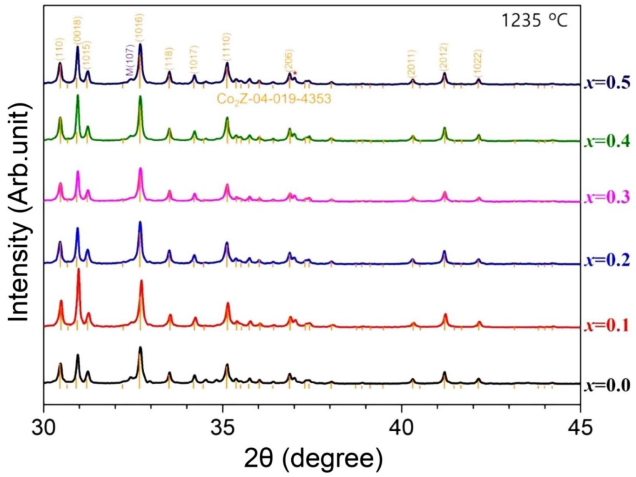


**Fig. 2.** (Color online) XRD patterns of $Sr_3Co_{2-x}Ni_xFe_{23}O_{41}$ ($x$ = 0, 0.1, 0.2, 0.3, 0.4, 0.5) hexaferrites calcined at 1235 °C.

conducted with the samples calcined at 1235 °C.

Figures 3(a)-(d) show SEM micrographs of $Sr_3Co_{2-x}Ni_x$-$Fe_{23}O_{41}$ hexaferrite powders ($x$ = 0.5) calcined at 1185-1250 °C, where the Z-type was the primary phase and

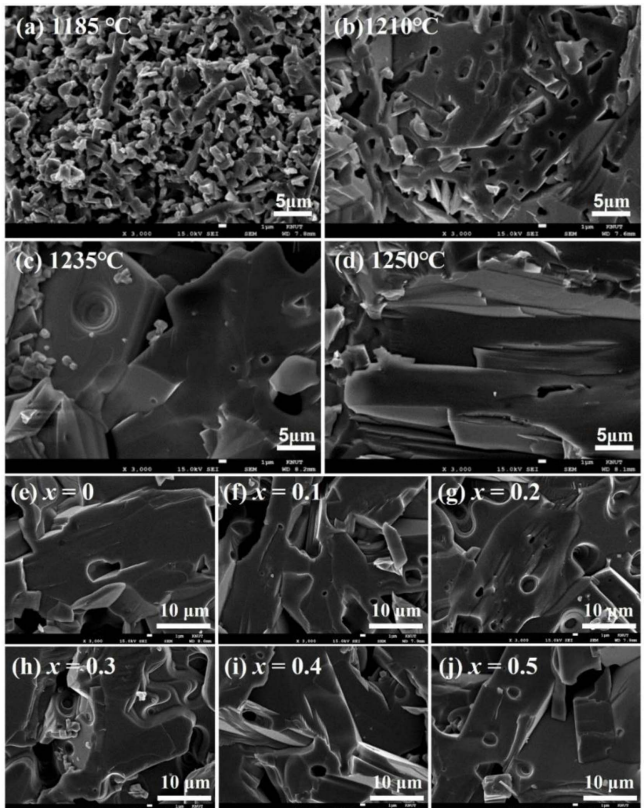


**Fig. 3.** SEM micrographs of (a-d) $Sr_3Co_{2-x}Ni_xFe_{23}O_{41}$ ($x$ = 0.5) hexaferrites calcined at 1185, 1210, 1235, 1250 °C, and (e-j) $Sr_3Co_{2-x}Ni_xFe_{23}O_{41}$ ($x$ = 0.1, 0.2, 0.3, 0.4, and 0.5) hexaferrites calcined at 1235 °C.

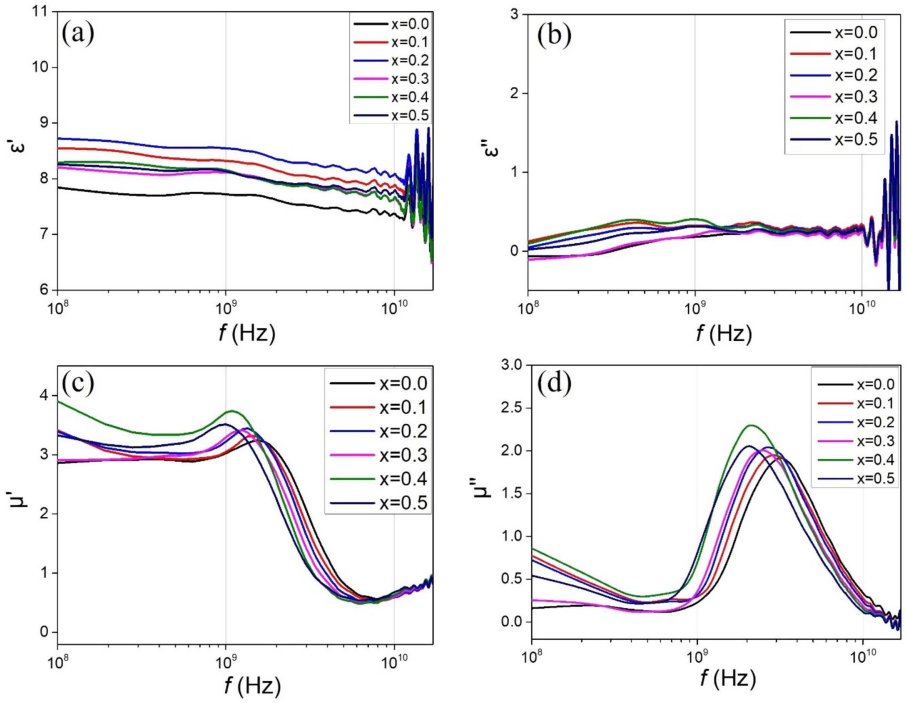


**Fig. 4.** (Color online) (a, b) Complex permittivity ($\varepsilon'$, $\varepsilon''$) and (c, d) permeability ($\mu'$, $\mu''$) spectra (100 MHz ≤ $f$ ≤ 18 GHz) of $Sr_3Co_{2-x}Ni_xFe_{23}O_{41}$ ($x$ = 0.1, 0.2, 0.3, 0.4, and 0.5) hexaferrite-epoxy (10 wt%) composites.

manually ground. At $T_{cal}$ = 1185 °C, the grain size was only a few micrometers. At $T_{cal}$ = 1210 °C, the grain grew significantly, and at $T_{cal}$ ≥ 1235 °C, it grew to a considerable size. The XRD data shown in Fig. 1 reveal that the M-phase was the primary phase at $T_{cal}$ = 1185 and 1210 °C, with the Z-phase partially included. The Z-type phase then became the primary phase at $T_{cal}$ = 1235 and 1250 °C. The samples with $T_{cal}$ = 1235 and 1250 °C had very large plate-shaped grains with a plate diameter greater than 10 μm. It is believed that Ni-substituted $Sr_3Co_2Z$ possesses sufficient driving force for large grain growth at temperatures greater than 1235 °C during calcination under a solid-state reaction. Regardless of the Ni substitution amount, all samples of $Sr_3Co_{2-x}Ni_xFe_{23}O_{41}$ ($x$ = 0.1, 0.2, 0.3, 0.4, and 0.5) hexaferrite showed similar large grain microstructures when calcined at 1235 °C (Fig. 3(e)-(j)). The abnormal grain growth phenomenon in Z-type hexaferrites was reported in a previous study [29], and the discontinuous grain growth mechanism could explain the anomalously large grain growth in hexaferrites.

The real and imaginary parts of the complex permittivity ($\varepsilon'$ and $\varepsilon''$) and permeability ($\mu'$ and $\mu''$) spectra of the $Sr_3Co_{2-x}Ni_xFe_{23}O_{41}$ ($x$ = 0.1, 0.2, 0.3, 0.4, and 0.5) hexaferrite-epoxy (10 wt%) composites are shown in Figs. 4(a)-(d). The $\varepsilon'$ spectra shown in Fig. 4(a) reveal that the ε' values of the samples ($x$ = 0.1, 0.2, 0.3, 0.4, and 0.5) were present in the range of 7-9 with no clear tendency on $x$. Fig. 4(b) shows that the $\varepsilon''$ values of the samples were in the range 0.1-0.4. The irregularities in the $\varepsilon'$ and $\varepsilon''$ spectra at $f$ > 10 GHz appeared to be noisy signals. Flat $\varepsilon'$ spectra with a fractional level of $\varepsilon''$ close to 0 are characteristic of an insulating material with no space charge involved. Fig. 4(c) shows that the $\mu'$ spectra exhibited clear transitions in the frequency range of 1-10 GHz and a gradual shift to the left (lower frequency) with an increase in $x$. Fig. 4(d) shows that the $\mu''$ spectra exhibited clear peaks in the frequency range of 2.0-3.2 GHz, and the peak frequency of $\mu''$ also gradually moved to a low frequency as $x$ increased. The gradual spectra shift can be attributed to the gradual decrease of magneto-crystalline anisotropy with increasing $x$ [17, 20-23]. Table 1 shows the real and imaginary parts of permittivity ($\varepsilon'$, $\varepsilon'$) and real part of permeability ($\mu'_s$) at 1 GHz, the maximum imaginary part of permeability ($\mu''_{max}$), and the frequencies of $\mu''_{max}$ ($f_{\mu''max}$) of the $Sr_3Co_{2-x}Ni_xFe_{23}O_{41}$ ($x$ = 0.1, 0.2, 0.3, 0.4, and 0.5) hexaferrite-epoxy (10 wt%) composites. In the hexaferrite, the $f_{\mu''max}$ exist in the GHz range can be considered to $f_{FMR}$.

RL, which represents the EM wave absorption performance, can be calculated using transmission line theory [31]. First, $\frac{Z_{in}}{Z_o}$ spectra at a specified thickness ($d$) should be obtained by substituting the values of $\varepsilon_r$ and $\mu_r$ spectra into the following equation:

**Table 1.** Real and imaginary parts of permittivity ($\varepsilon'$, $\varepsilon'$), and real part of permeability ($\mu'_s$) at 1 GHz, maximum imaginary part of permeability ($\mu''_{max}$), frequency $\mu''_{max}$, minimum RL ($RL_{min}$), frequency of $RL_{min}$ ($f_{RLmin}$), and thickness of $RL_{min}$ ($d_{RLmin}$) of the $Sr_3Co_{2-x}Ni_xFe_{23}O_{41}$ ($x$ = 0.1, 0.2, 0.3, 0.4, and 0.5) hexaferrite-epoxy (10 wt%) composites.

| $x$ | $\varepsilon'$ (@1 GHz) | $\varepsilon''$ (@1 GHz) | $\mu'_S$ (@1 GHz) | $\mu''_{max}$ | $f_{\mu''max}$ (GHz) | $RL_{min}$ (dB) | $f_{RLmin}$ (GHz) | $d_{RLmin}$ (mm) |
|---|---|---|---|---|---|---|---|---|
| 0.0 | 7.70 | 0.187 | 3.08 | 1.92 | 3.14 | -48.3 | 3.23 | 4.6 |
| 0.1 | 8.31 | 0.324 | 3.11 | 1.95 | 2.87 | -42.7 | 2.87 | 4.9 |
| 0.2 | 8.54 | 0.315 | 3.30 | 2.04 | 2.70 | -49.5 | 2.70 | 5.1 |
| 0.3 | 8.10 | 0.221 | 3.37 | 2.01 | 2.52 | -38.6 | 2.61 | 5.5 |
| 0.4 | 8.12 | 0.399 | 3.74 | 2.30 | 2.07 | -46.2 | 2.34 | 5.7 |
| 0.5 | 8.10 | 0.315 | 3.48 | 2.06 | 2.07 | -41.3 | 2.25 | 6.3 |

$$\frac{Z_{in}}{Z_o} = \sqrt{\frac{\mu_r}{\varepsilon_r}} \tanh\left[ j\left(\frac{2\pi f d}{c}\right)\sqrt{\mu_r \varepsilon_r}\right], \quad (1)$$

where $Z_{in}$ is the input impedance of the absorber, $Z_0 = \sqrt{\mu_0 \varepsilon_0}$ is the characteristic impedance of free space, $c$ is the speed of light, $f$ is the frequency of the incident EM wave, $d$ is the thickness of the absorber, and $\mu_r = \mu' - j\mu''$ and $\varepsilon_r = \varepsilon' - j\varepsilon''$ are complex numbers. Then, the RL spectra at a specified $d$ can be obtained by inputting the $\frac{Z_{in}}{Z_o}$ into

$$RL(dB) = 20\log\left|\frac{\frac{Z_{in}}{Z_o} - 1}{\frac{Z_{in}}{Z_o} + 1}\right|, \quad (2)$$

The measured $\mu'$, $\mu''$, $\varepsilon'$, and $\varepsilon''$ spectra shown in Figs. 4(a)-(d) can then be used to obtain $\frac{Z_{in}}{Z_o}$ for any thickness $d$ with respect to $f$. For the most effective EM wave absorption, the impedance matching conditions in which the $\frac{Z_{in}}{Z_o}$ value in Eq. (2) approaches 1 should be satisfied.

RL spectra for an absorber thickness of $0 \le d \le 10$ mm were calculated and plotted in square $f$–$d$ maps for $Sr_3Co_{2-x}Ni_xFe_{23}O_{41}$ ($x$ = 0.1, 0.2, 0.3, 0.4, and 0.5) hexaferrite-epoxy (10 wt%) composites, as shown in Figs. 5(a)-(f). The area in which RL ≤ –10 dB, which suggests EM wave absorptions greater than 90%, is outlined in black solid lines. In this area, the regions where RL ≤ –20, –30, and –40 dB are outlined with solid lines. Table 1 lists the values for the minimum RL ($RL_{min}$), frequency of $RL_{min}$ ($f_{RLmin}$), and thickness of $RL_{min}$ ($d_{RLmin}$). The RL

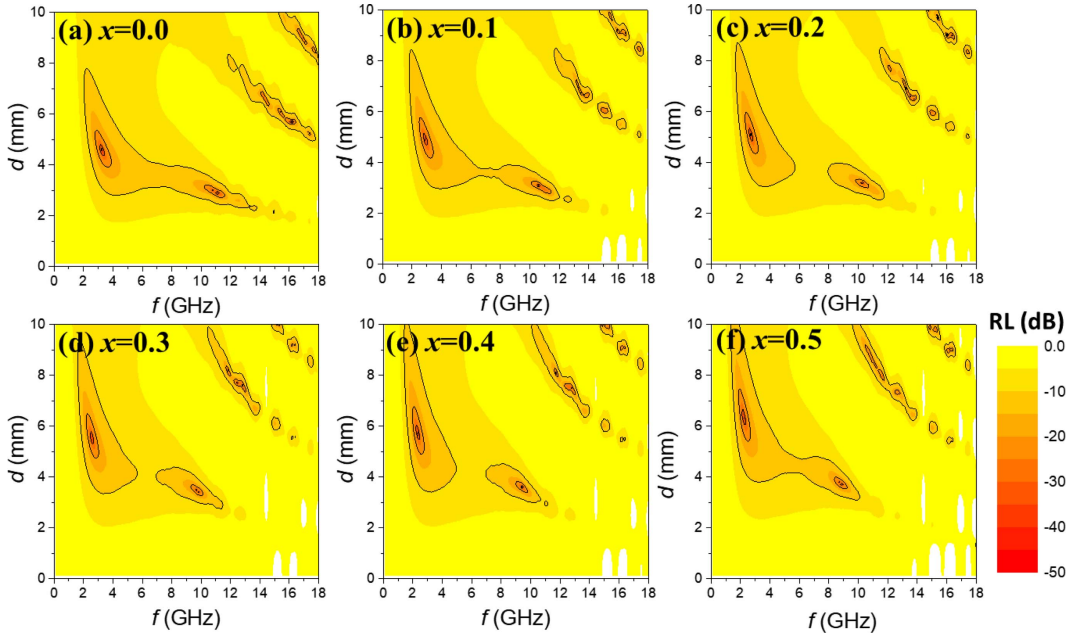


**Fig. 5.** (Color online) RL maps of $Sr_3Co_{2-x}Ni_xFe_{23}O_{41}$ ($x$ = 0.1, 0.2, 0.3, 0.4, and 0.5) hexaferrite-epoxy (10 wt%) composites.

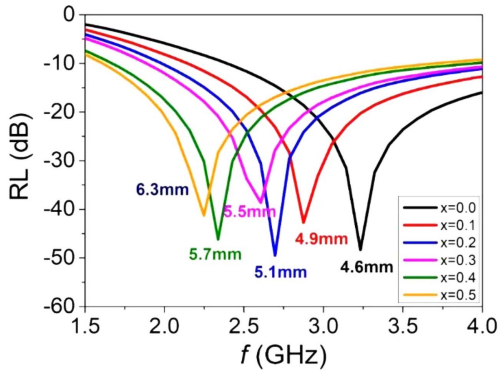


**Fig. 6.** (Color online) RL spectra of $Sr_3Co_{2-x}Ni_xFe_{23}O_{41}$ ($x$ = 0.1, 0.2, 0.3, 0.4, and 0.5) hexaferrite-epoxy (10 wt%) composites at the optimal thickness for each sample.

maps show similar absorption patterns. The strongest absorption area was in the frequency and thickness ranges of 2-4 GHz and 4-6 mm, respectively; the second strongest absorption area was in the ranges of 8-10 GHz and 3-4 mm, respectively. Note that the first strong EM wave absorption area corresponds to $\mu''$ at a frequency near $f_{\mu''max}$, and thus, the first $f_{RLmin}$ changed according to the gradual change in $f_{\mu''max}$ induced by the increase in Ni substitution $x$. Fig. 6 plots the RL spectra at the thickness at which the minimum RL point existed for each sample. $f_{RLmin}$ was 3.23 at $x$ = 0 and gradually decreased to 2.25 as $x$ increased to 0.5. All samples showed excellent EM absorption performance with an $RL_{min}$ value in the range of −35 to −50 dB. In addition, it was found that the second-strongest EM wave absorption frequency moved from ~11 GHz to 9 GHz with an increase in $x$ from 0 to 0.5. In our previous study on Z-type hexaferrites, we determined that the second EM absorption area originated from the ridge area of the $\mu''$ spectra (Fig. 4(d)) at frequencies greater than 8 GHz. This was because good impedance matching conditions are commonly satisfied at the first and second $RL_{min}$ points, where the $\frac{Z_{in}}{Z_o}$ value in Eq. (2) approaches unity.

## 4. Conclusions

In this study, Ni-substituted $Sr_3Co_2Z$ with a nominal cation composition of $Sr_3Co_{2-x}Ni_xFe_{23}$ ($x$ = 0, 0.1, 0.2, 0.3, 0.4, and 0.5) was prepared by solid-state reaction processes. Nearly single Z-type hexaferrites with the highest Ni solubility of $x$ = 0.5 were obtained when the samples were calcined at 1235 ºC. Following calcination, SEM micrographs revealed that all samples exhibited an abnormal growth of large grains (> 10 μm). For the ground hexaferrite powder-epoxy (10 wt%) composites, high-frequency complex permittivity ($\varepsilon'$, $\varepsilon''$) and permeability ($\mu'$, $\mu''$) spectra were measured, and the RL spectra were calculated based on transmission line theory. With increasing Ni substitution $x$, the permeability spectra gradually shifted to a low frequency. The $f_{\mu''max}$ and $f_{RLmin}$ gradually decreased from 3.14 GHz to 2.07 GHz and from 3.23 GHz to 2.25 GHz, respectively. The RL maps plotted as functions of $d$ and $f$ showed unique absorption patterns with first- and second-strongest EM absorption areas, and they were delicately tunable by the Ni substitution amount. These can be applied to S-band (2-4 GHz) and X-band (8-12 GHz) EM wave absorption, respectively.

## Acknowledgments

This study was supported by Basic Science Research Capacity Enhancement Project (National Research Facilities and Equipment Center) through the Korea Basic Science Institute funded by the Ministry of Education (Grant No. 2019R1A6C1010047) and by the Korea Basic Science Institute (National research Facilities and Equipment Center) grant funded by the Ministry of Education (grant No. 2021R1A6C103A367).

## References

[1] R. C. Pullar, Prog. Mater. Sci. **57**, 1191 (2012).
[2] L. B. Kong, Z. W. Li, L. Liu, R. Huang, M. Abshinova, Z. H. Yang, C. B. Tang, P. K. Tan, C. R. Deng, and S. Matitsine, Inter. Mater. Rev. **28**, 203 (2013).
[3] S. B. S. Magham, M. Sharma, S. R. Shannigrahi, H. R. Tan, V. Sharma, Y. S. Meng, S. Idapalpati, R. V. Ramanujan, and D. V. M. Repaka, J. Magn. Magn. Mater. **441**, 303 (2017).
[4] J. Shen, K. Chen, L. Li, W. Wang, and Y. Jin, J. Alloy. Comp. **615**, 488 (2014).
[5] W. Lee, Y.-K. Hong, J. Park, G. LaRochelle, and J. Lee, J. Magn. Magn. Mater. **414**, 194 (2016).
[6] Wu, H. Su, Q. Ding, H. Zhang, Y. Jing, and X. Tang, Phys. B **429**, 85 (2013).
[7] S.-E. Lee, H.-J. Kim, J.-H. Lee, K.-S. Oh, H. T. Hahn, and J.-W. Choi, Mater. Lett. **187**, 94 (2017).
[8] N. Neveu, Y.-K. Hong, J. Lee, J. Park, G. Abo, W. Lee, and D. Gillespie, IEEE Trans. Magn. **49**, 4265 (2013).
[9] O. Kimura, K. Shoji, and H. Maiwa, J. Eur. Ceram. Soc. **26**, 2845 (2006).
[10] M.-H. Park and Y.-M. Kang, J. Magn. Magn. Mater. **491**, 165628 (2019).
[11] J. Verwell, Magnetic Properties of Materials (ed. J. Smit), New York, McGraw-Hill, **64** (1971).
[12] R. Kuchi, V. Dongquoc, D. Kim, S.-G. Yoon, S.-Y. Park, and J.-R. Jeong, Met. Mater. Int. **23**, 405 (2017).
[13] R. Kuchi, V. Dingquoc, S. Surabhi, D. Kim, S.-G. Yoon,

S.-Y. Park, J. Choi, and J.-R. Jeong, Phys. Status Solidi A (2018) 1701032.
[14] R. Kuchi, M. Sharma, S. W. Lee, D. Kim, N. Jung, and J.-R. Jeong, Prog. Nat. Sci. Mater. Inter. **29**, 88 (2019).
[15] R. Kuchi, V. Dongquoc, P. C. Van, D. Kim, and J.-R. Jeong, J. Environ. Chem. Eng. **9**, 106585 (2021).
[16] P. Singh, V. K. Babbar, A. Razdan, R. K. Puri, and T. C. Goel, J. Appl. Phys. **87**, 4362 (2000).
[17] J.-K. Kim, P.-Y. Yu, and Y.-M. Kang, J. Magn. Magn. Mater. **537**, 168235 (2021).
[18] A. Kumar and S. Singh, Mater. Sci. Eng. **330**, 012006 (2018).
[19] E.-S. Lim and Y.-M. Kang, Mater. Today Comm. **25**, 101411 (2020).
[20] E.-S. Lim, H. K. Kim, and Y.-M. Kang, J. Magn. Magn. Mater. **517**, 167397 (2021).
[21] P.-Y. Yu and Y.-M. Kang, Curr. Appl. Phys. **31**, 99 (2021).
[22] N. Raju, S. S. K. Reddy, J. Ramesh, Ch. G. Reddy, P. Y. Reddy, K. R. Reddy, V. G. Sathe, and V. R. Reddy, J. Appl. Phys. **120**, 054103 (2016).
[23] J.-H. Heo, J.-Y. Yoo, and Y.-M. Kang, J. Magn. Magn. Mater. **550**, 169051 (2022).
[24] Z. W. Li, Y. P. Wu, G. Q. Lin, and L. F. Chen, J. Magn. Magn. Mater. **310**, 145 (2007).
[25] M. A. Vinnik, Russ. J. Inorg. Chem. **10**, 1164 (1965).
[26] J. Li, H.-F. Zhang, G.-Q. Shao, D. Chen, G.-G. Zhao, Z.-S.Gao, J.-H. Liu, J.-S. Lu, and X.-B. Li, Proc. Eng. **102**, 1885 (2015).
[27] J.-T. Lim, I.-B. Shim, E. J. Hahn, and C. S. Kim, AIP Adv. **7**, 056108 (2017).
[28] E.-S. Lim, T.-W. Hong, and Y.-M. Kang, J. Kor. Magn. Soc. **30**, 31 (2020).
[29] E. S. Al-Hwaitat, S. M. Mahmood, M. Al-Hussein, and I. Bsoul, Adv. Mater. Sci. Eng. **2018**, 6152020 (2018).
[30] E. S. Al-Hwaitat, M. A. Hussein, I. Bsoul, R. A. Buqain, and S. H. Mahmood, Acta. Phys. Pol. A **136**, 548 (2019).
[31] Y. Naito and K. Suetake, IEEE Trans. Microw. Theory Tech. **19**, 65 (1971).